Imaging tunable Luttinger liquid systems in van der Waals heterostructures

https://doi.org/10.1038/s41586-024-07596-6

Received: 25 December 2023

Accepted: 23 May 2024

Hongyuan Li[1,2,3,8] ✉, Ziyu Xiang[1,2,3,8], Tianle Wang[1,3,8], Mit H. Naik[1,3,8], Woochang Kim[1,3], Jiahui Nie[1], Shiyu Li[1], Zhehao Ge[1], Zehao He[1], Yunbo Ou[4], Rounak Banerjee[4], Takashi Taniguchi[5], Kenji Watanabe[6], Sefaattin Tongay[4], Alex Zettl[1,3,7], Steven G. Louie[1,3] ✉, Michael P. Zaletel[1] ✉, Michael F. Crommie[1,3,7] ✉ & Feng Wang[1,3,7] ✉

One-dimensional (1D) interacting electrons are often described as a Luttinger liquid[1–4] having properties that are intrinsically different from those of Fermi liquids in higher dimensions[5,6]. In materials systems, 1D electrons exhibit exotic quantum phenomena that can be tuned by both intra- and inter-1D-chain electronic interactions, but their experimental characterization can be challenging. Here we demonstrate that layer-stacking domain walls (DWs) in van der Waals heterostructures form a broadly tunable Luttinger liquid system, including both isolated and coupled arrays. We have imaged the evolution of DW Luttinger liquids under different interaction regimes tuned by electron density using scanning tunnelling microscopy. Single DWs at low carrier density are highly susceptible to Wigner crystallization consistent with a spin-incoherent Luttinger liquid, whereas at intermediate densities dimerized Wigner crystals form because of an enhanced magneto-elastic coupling. Periodic arrays of DWs exhibit an interplay between intra- and inter-chain interactions that gives rise to new quantum phases. At low electron densities, inter-chain interactions are dominant and induce a 2D electron crystal composed of phased-locked 1D Wigner crystal in a staggered configuration. Increased electron density causes intra-chain fluctuation potentials to dominate, leading to an electronic smectic liquid crystal phase in which electrons are ordered with algebraical correlation decay along the chain direction but disordered between chains. Our work shows that layer-stacking DWs in 2D heterostructures provides opportunities to explore Luttinger liquid physics.

Landau's Fermi liquid theory has been successful in describing interacting electrons in two and three dimensions using concepts based on Fermionic quasiparticle excitations[5,6]. However, this picture fails for interacting electrons confined to one dimension and leads to Luttinger liquid behaviour[1–4], in which the elementary excitations are bosonic. The one-dimensional (1D) electron interaction strength and resulting Luttinger liquid behaviour can be tuned continuously by varying the electron density. Isolated 1D electron chains at high electron density are well described by a weakly interacting Luttinger liquid theory[2–4] (that is, in which the electron interactions are relatively weak). This description features spin–charge separation in which low-energy excitations are described by plasmons and spinons. In the low-density limit, however, 1D electrons cross over into a regime that features a high susceptibility to quasi-long-range Wigner crystallization because of stronger electron interactions. This regime has a qualitatively different picture for spin–charge separation, in which the charge mode is described as an electron crystal phonon and the spin mode is determined by antiferromagnetic exchange coupling between the nearest-neighbour electrons[7,8]. Here spin exchange interactions are highly suppressed and thermal fluctuations dominate, making the system a spin-incoherent Luttinger liquid[7,8]. For intermediate electron densities, the spin exchange interaction can lead to an unusual form of magneto-elastic coupling[7,8], in which the electron lattice dimerizes and forms valence-bond spin-singlet pairs to lower the overall magnetic energy (that is, the spin-Peierls effect), analogous to the Su–Schrieffer–Heeger model. The electron crystal ultimately evolves into a standard linear Luttinger liquid as spin and charge energies become comparable at sufficiently high electron density. Because crystalline order is algebraic in one dimension, the evolution from low to high density is a crossover. Arrays of 1D electron chains host even richer phenomena because of the interplay between intra- and inter-chain interactions. Depending on the strength of inter-chain interactions, many new quantum phases have been predicted theoretically, including two-dimensional (2D) electron crystals[9,10], electron smectic liquid crystals[10] and even sliding Luttinger liquids exhibiting non-Abelian fractional quantum Hall states[11,12].

---

[1]Department of Physics, University of California at Berkeley, Berkeley, CA, USA. [2]Graduate Group in Applied Science and Technology, University of California at Berkeley, Berkeley, CA, USA. [3]Materials Sciences Division, Lawrence Berkeley National Laboratory, Berkeley, CA, USA. [4]School for Engineering of Matter, Transport and Energy, Arizona State University, Tempe, AZ, USA. [5]International Center for Materials Nanoarchitectonics, National Institute for Materials Science, Tsukuba, Japan. [6]Research Center for Functional Materials, National Institute for Materials Science, Tsukuba, Japan. [7]Kavli Energy Nano Sciences Institute at the University of California Berkeley and the Lawrence Berkeley National Laboratory, Berkeley, CA, USA. [8]These authors contributed equally: Hongyuan Li, Ziyu Xiang, Tianle Wang, Mit H. Naik. ✉e-mail: hongyuan_li@berkeley.edu; sglouie@berkeley.edu; mikezaletel@berkeley.edu; crommie@berkeley.edu; fengwang76@berkeley.edu

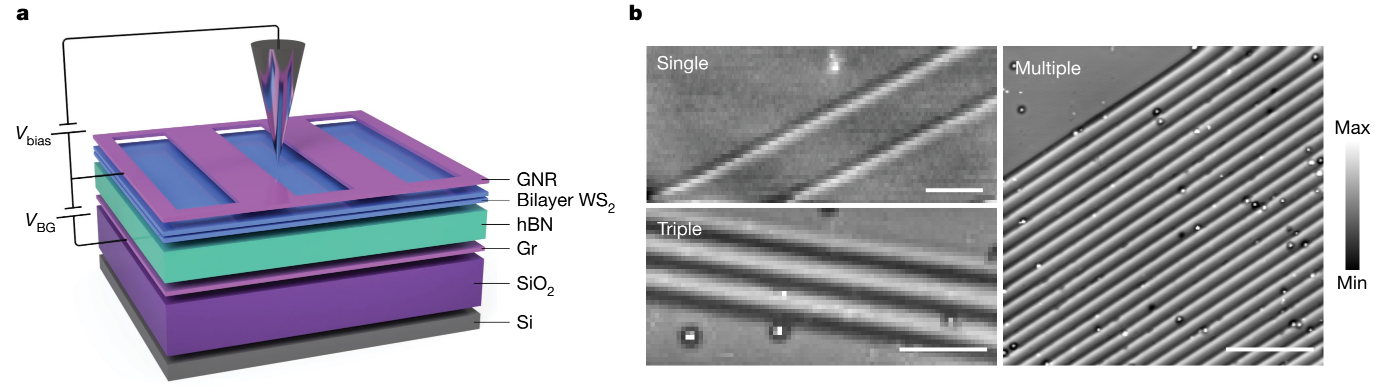

Fig. 1 | Stacking DWs in a bilayer WS_2. a, Schematic of the STM measurement of a gate-tunable bilayer WS_2 device. The bilayer WS_2 is placed on top of a 67-nm thick hBN layer and a graphite substrate that defines the back gate. A back gate voltage V_{BG} is applied to perform electron-doping of the WS_2. A sample-tip bias V_{bias} is applied to the WS_2 and relative to the STM tip. A GNR array is placed on top of the WS_2 to serve as the contact electrode. **b**, Typical STM topographic images of the stacking DWs in the bilayer WS_2 that separates two AB stacking regions with a one-unit-vector interlayer dislocation. The DWs exhibit different aggregation behaviours, including single DWs (left top), triple DWs (left bottom) and DW periodic arrays (right). The inter-DW distance in the triple DWs and DW arrays is about 8 nm. Max, maximum; Min, minimum. Scale bars, 20 nm (**b**, left top and left bottom); 50 nm (**b**, right).

In the past few decades, efforts have been made to explore Luttinger liquids experimentally. Weakly interacting Luttinger liquids have been observed in 1D metals[13,14], semiconductor nanowires[15–18], topological edges states[19–22] and twin-boundary defects[23,24], in which spin–charge separation and power-law scaling of tunnelling probability have been observed. Characterizing strongly interacting 1D electrons at lower densities is more difficult because they are sensitive to inevitable weak disorder and stray fields. Suspended semiconducting carbon nanotubes have provided a useful platform to explore the low-density regime, and signatures of Wigner crystallization have been observed in carbon nanotube electrical transport[25] and scanning single-electron transistor (SET) measurements[15]. However, even few-electron Wigner crystals in these nanotubes are strongly distorted by disorder, thus preventing the study of quasi-long-range order and the crossover from a strongly interacting Wigner crystal to a weakly interacting Luttinger liquid. Experimentally characterizing arrays of coupled Luttinger liquids is even more challenging for lack of a suitable platform. It has been suggested that the stripe phase of high-temperature superconductors[26] and the anisotropic moire superlattice in twisted WTe_2 (ref. 27) might provide coupled 1D electron chains, but microscopic descriptions of these materials are still lacking.

Here we demonstrate that layer-stacking domain walls (DWs) in bilayer WS_2 form an ideal platform for exploring spin and orbital quantum behaviour in 1D Luttinger liquids with tunable interaction strength. Stacking DWs can be formed either in isolated form (yielding single 1D electron chains) or as self-assembled periodic arrays of Luttinger liquids. An advantage of DWs is that they are embedded in 2D van der Waals heterostructures that exhibit low structural disorder and facilitate convenient electrical device fabrication and characterization. Using scanning tunnelling microscopy (STM), we have directly imaged the evolution of DW-based Luttinger liquids under different interaction regimes that reveal new quantum phenomena. We find that isolated DWs exhibit almost perfect 1D Wigner crystals pinned by dilute defects at low electron density. In this regime, density matrix renormalization group (DMRG) calculations suggest that exponentially suppressed spin interactions are dominated by thermal excitations for our experimental temperature, giving rise to spin-incoherent Luttinger liquid behaviour. At increased electron densities, we experimentally observe dimerized Wigner crystals that are consistent with theoretical predictions of enhanced magneto-elastic coupling between an antiferromagnetic spin chain and the electron charge lattice. Our DMRG calculations in this regime suggest that this dimerization is associated with enhanced susceptibility to oscillating valence bond order. At even higher density, the observed Wigner crystals evolve into weak-interacting linear Luttinger liquids both experimentally and in our calculations. For periodic arrays of DWs in the low-electron-density regime, we experimentally observe anisotropic 2D electron lattice behaviour arising from phase-locked 1D Wigner crystals. At increased densities, a new electron smectic liquid crystal phase emerges.

Device and measurement scheme

Our experimental setup involves an artificially stacked 60°-twisted bilayer WS_2 device integrated into a scanning tunnelling microscope as shown in Fig. 1a (see Methods for fabrication details). The artificial stacking technique introduces small angle variations and strain that generate stacking DWs in the bilayer WS_2. The bilayer WS_2 is placed on top of an hBN flake with thickness $d_{hBN} = 67$ nm that is placed above a graphite back gate. A back gate voltage V_{BG} is applied to electrostatically dope electrons into the bilayer WS_2. A sample-tip bias V_{bias} is applied enabling the STM measurement. We use a graphene nanoribbon (GNR) contact electrode on the WS_2 surface to minimize the device resistance and facilitate STM measurement[28].

Our STM topographic images of bilayer WS_2 (Fig. 1b) show a series of 1D structures corresponding to stacking DWs. A single DW separates two AB stacking regions with in-plane dislocations of one unit cell characterized by a Burgers vector[29–35] (see Methods and Extended Data Fig. 1 for more details). We observe different DW configurations, including isolated DWs (Fig. 1b, top left) and few-DW clusters (Fig. 1b, bottom left). DWs are also observed to self-assemble into periodic arrays (Fig. 1b, right) with inter-DW separation of $L_{DW} \approx 8.2$ nm. Combining density functional theory (DFT) calculations with our STM spectroscopy shows that the conduction band minimum in a DW is lower than for an AB stacked region (see Supplementary Information sections 3 and 4 for more details). This causes electrostatically doped electrons (controlled by the back gate voltage) to be confined within the DWs and thus provides a platform for studying Luttinger liquids.

Wigner–Friedel crossover in isolated DWs

We are able to directly image the electron distribution in DWs by measuring the tunnel current from DW conduction band edge (CBE) states[36] (see Methods and Extended Data Fig. 2 for details). Figure 2a shows the

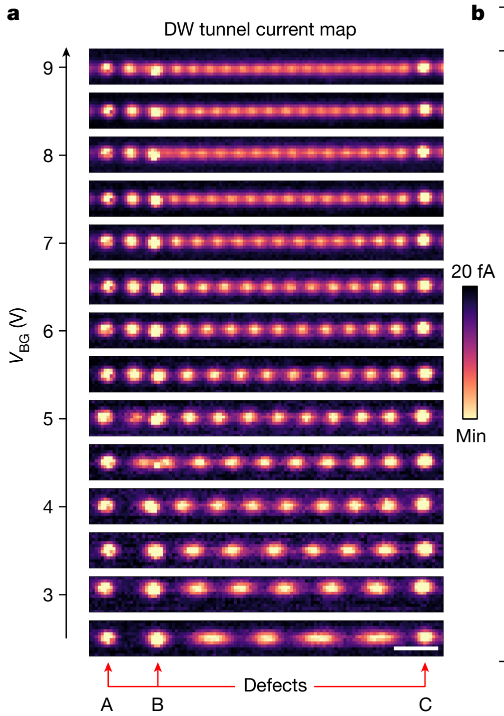

b

d (nm)	r_s
3.8	7.2
4.0	7.6
4.1	7.8
4.3	8.1
4.6	8.7
5.0	9.4
5.4	10.2
6.0	11.3
6.7	12.7
7.1	13.4
7.5	14.2
8.6	16.3
10.0	18.9
12.0	22.7

Fig. 2 | Tunnel current measurement of 1D Wigner crystal. a, CBE tunnel current maps for the centre DW in a triple-DW group with V_{BG} increased from 2.5 V to 9.0 V. V_{bias} is selected in the range of $-0.85\ V < V_{bias} < -0.30$ V to minimize the tip-sample vacuum level mismatch (tip setpoint: $V_{bias} = -2.70$ V, $I_{sp} = 20$ pA, and $h_{tip} = -100$ pm). The maps show a pinned 1D Wigner crystal in which each bright dot corresponds to one localized electron. Three pinning defects are labelled with red arrows at the bottom. **b**, Table of the electron separations and corresponding values of r_s for the images shown in **a**. Min, minimum. Scale bar, 10 nm (**a**).

evolution of the CBE tunnel current map for a DW (central one in triple DWs) in the low-electron-density regime for $2.5\ V < V_{BG} < 9.0$ V. Three bright spots labelled as A, B and C remain fixed even as the electron density is changed and are attributed to three separate defects in the DW that each pin an electron. Between defects B and C, we observe a periodic lattice of highly localized electrons with a quantized electron number that increases from 4 to more than 15 as V_{BG} is increased from 2.5 V to 9.0 V. This tunable 1D electron lattice provides direct evidence for 1D Wigner crystal formation in DWs. Although a true crystal with long-range order is theoretically forbidden in an infinite 1D system, a well-defined Wigner crystal with quasi-long-range order can be stabilized by long-range Coulomb interactions in a finite 1D chain[37], as observed here.

The observed 1D electron lattices show almost no disorder except for the defects pinning the ends of the Wigner crystal chain, thus indicating the high quality of the 1D DW system. The Wigner crystal persists to a surprisingly high electron density. We can characterize the electron density using the dimensionless parameter $r_s = \frac{d}{a_B}$ where d is the electron separation, $a_B = \frac{4\pi\varepsilon\hbar^2}{m_e e^2}$ is the effective Bohn radius, $m_e = 0.39m_0$ is the effective electron mass obtained from our DFT calculations and $\varepsilon = 3.9\varepsilon_0$ is the relative permittivity (ε_0 is the vacuum permittivity). The values of d and r_s for the 1D lattice shown in Fig. 2a are listed in the table of Fig. 2b and stand in contrast to the case of 2D electron gases in which the Wigner crystal state exists only for $r_s > 30$ (refs. 38–40). We see that the 1D Wigner crystal state is present for our DW lengths even at $r_s < 8$. This is a signature of the strong impact that electron–electron interactions have in 1D.

At increased electron densities, a crossover from the 1D Wigner crystal to a dimerized Wigner crystal and then to a weakly interacting Luttinger liquid is observed. Figure 3a shows the evolution of the CBE tunnel current map for 1D electrons in a DW containing a single defect over the range $8.5\ V < V_{BG} < 14.5$ V. For better visualization of the experimental data, Fig. 3b shows a 2D plot of the normalized current as a function of V_{BG} and horizontal position in which each horizontal line is obtained by vertically averaging the pixels for each image in Fig. 3a. Wigner crystal formation is seen at low electron densities, but as V_{BG} is raised above 10 V an unexpected distortion of the Wigner crystal is observed in which adjacent peaks merge and form dimers. The dimerization becomes more pronounced at increased electron density until V_{BG} reaches about 11.5 V, at which point the two peaks in each dimer pair merge into a single broad peak. For $V_{BG} > 11.5$ V, the Wigner crystal is gone and a new pattern with a doubled period emerges. This new pattern corresponds to the charge density oscillation (that is, Friedel oscillation) of a Luttinger liquid in the weakly interacting regime.

The crossover from Wigner crystal to weakly interacting Luttinger liquid can also be seen in momentum space. Figure 3c shows the fast Fourier transformation (FFT) of Fig. 3b and exhibits two distinct wavevector peaks at different electron densities. In a non-interacting two-fold degenerate 1D system (that is, due to spin-valley locking) the Fermi wavevector is $k_F = \frac{\pi N}{2L}$, where L is the 1D chain length and N is the total electron number. The Friedel oscillation (also present in the non-interacting limit) arising from the backscattering of electrons then has a wavevector $k_{Fr} = 2k_F = \frac{\pi N}{L}$. By contrast, the Wigner crystal state has a period of L/N and thus features a wavevector $k_W = \frac{2\pi N}{L} = 4k_F$. The two dispersive peaks in Fig. 3c are, therefore, assigned to the Wigner crystal (red dashed line) and Friedel oscillation (white dashed line). The Wigner crystal branch ($4k_F$) becomes weaker with increased electron density and disappears at $V_{BG} \approx 11.5$ V. The Friedel oscillation branch ($2k_F$) emerges at $V_{BG} \approx 10$ V and becomes the dominant periodicity gradually with the increased electron density. Both branches are seen in the intermediate region $10\ V < V_{BG} < 11.5$ V, which corresponds to the dimerized Wigner crystal regime. Extended data showing the crossover from Wigner crystal to weakly interacting Luttinger liquid are included in Supplementary Information section 5.

To better understand the different density-dependent regimes observed experimentally for isolated DWs, we performed numerical DMRG calculations (see Supplementary Information section 6 for details). Figure 3d shows the resulting local electron density profile as a function of average density for a DMRG calculation of a finite 1D chain of electrons at $T = 0$. The corresponding FFT plot is shown in Fig. 3e. Comparison of Fig. 3d,e with Fig. 3b,c shows that the DMRG calculation captures the main features of the experiment, including the dimerization of the Wigner crystal with increasing electron density followed by a crossover into the weakly interacting Luttinger liquid regime featuring a $2k_F$ oscillation.

The DMRG result shows the $2k_F$ oscillation (Fig. 3e) extending further into the low-density regime than is seen experimentally (Fig. 3c). This probably originates from the thermal excitation of the spin degree of freedom at low density during the experiment ($T = 5.4$ K) (see Methods and Extended Data Fig. 3a for details). This regime has been theoretically explored previously and is referred to as a spin-incoherent Luttinger liquid[7,8] in which thermally induced spin incoherence suppresses the $2k_F$ Friedel oscillation relative to the $4k_F$ Wigner crystal[7,8], consistent with our experimental data.

The dimerization phenomenon occurring at slightly higher density ($0.30\ \mathrm{nm}^{-1} < n < 0.38\ \mathrm{nm}^{-1}$; Fig. 3b,c) arises when the spin exchange energy exceeds the thermal energy, thus making the spin behaviour important in the Wigner crystal. In this regime, the electrons are antiferromagnetically coupled, and the exchange energy strongly depends on the electron separation, leading to a magneto-elastic coupling which tends to lower the overall energy of the 1D system by dimerizing the lattice to gain magnetic energy (see Methods and Extended Data Fig. 3b,c for details).

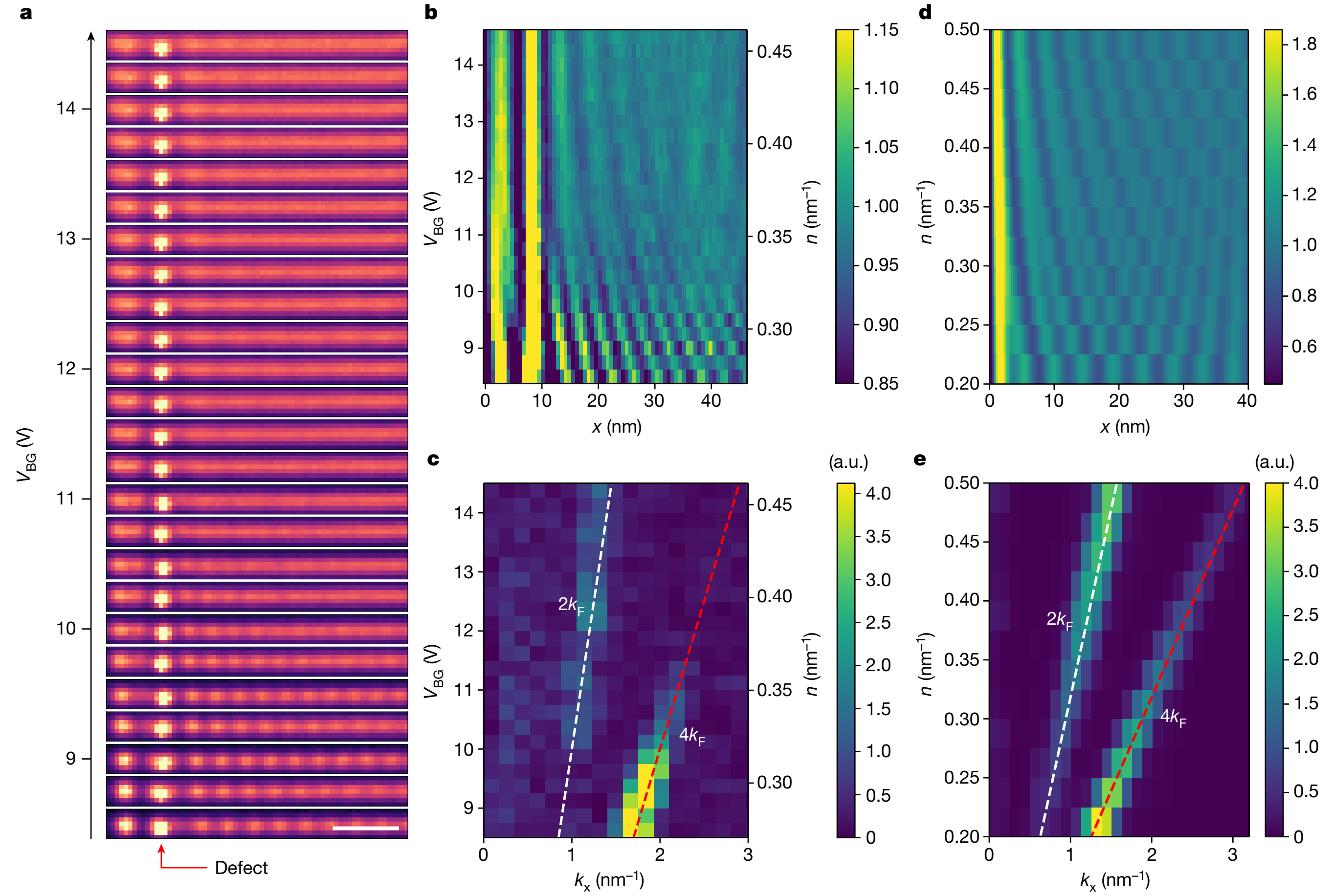

Fig. 3 | One-dimensional Wigner–Friedel crossover. a, Evolution of CBE tunnel current maps for a centre DW in a triple-DW group with V_{BG} increased from 8.5 V to 14.5 V. The periodic structure of the 1D Wigner crystal is gradually replaced by a new periodic structure having twice the period. A defect near the left end is labelled with a red arrow. $V_{bias} = -0.23$ V (tip setpoint: $V_{bias} = -2.70$ V, $I_{sp} = 20$ pA and $h_{tip} = -100$ pm). **b**, 2D plot of the normalized CBE tunnel current of the DW in **a**. Each line comes from vertically averaging the pixels of an image from **a**. **c**, FFT of the data shown in **b**. A Hamming window was used for the FFT. Two dispersing peaks (labelled with dashed lines) correspond to $2k_F$ and $4k_F$, where k_F is the Fermi wavevector as defined in the text. **d**, DMRG calculation of the 1D spatial charge distribution as a function of electron density n. The simulated 1D chain is 80 nm long with hard-wall ends. The charge distribution is symmetric about $x = 40$ nm, so we only show the results for $x < 40$ nm. **e**, FFT of the result shown in **d**. Dispersing peaks at $2k_F$ and $4k_F$ can be seen. Scale bar, 10 nm (**a**).

In the high-density regime ($n > 0.38$ nm^{-1}), the electron kinetic energy overcomes the Coulomb interaction, and the system behaves as a weakly interacting Luttinger liquid. Here the electron density is dominated by the $2k_F$ Friedel oscillation, and the $4k_F$ oscillation gradually vanishes because of the delocalization of the Wigner crystal.

Intra- and inter-chain interactions in DW arrays

The interactions between 1D electron chains in DW arrays lie beyond the scope of our 1D DMRG treatment, but this is also a regime in which we observe rich experimental phenomenology, including new quantum phases arising from the interplay between intra- and inter-DW interactions. Figure 4a–h shows the experimental evolution of the CBE tunnel current for an array of DWs as V_{BG} is increased over the range 2.0 V < V_{BG} < 5.0 V. We find that the distribution of electrons across the DWs changed dramatically as the overall density is changed. At low electron density (Fig. 4a–d), the DW Wigner crystal chains exhibit a staggered structure with electrons in one chain aligning with empty sites in the neighbouring chain. This can be seen in the blue arrows of Fig. 4c that trace the zigzag path between electrons in neighbouring chains (defects are identified by yellow circles in Fig. 4g). The staggered structure minimizes inter-DW interactions (that is, by maximizing the separation between electrons in neighbouring DWs) thus producing a new anisotropic 2D electronic crystalline phase. Figure 4i–l shows 2D FFT plots of the low-density staggered phase shown in Fig. 4a–d. Sharp diffraction peaks characterizing this new crystalline phase can be observed.

At higher electron density (Fig. 4e–h), the staggered electronic phase dissociates into a new electronic configuration. This can be seen in a trace of neighbouring electrons for $V_{BG} = 4.0$ V, which shows an almost random path (Fig. 4f, blue arrows). In this regime, a pinned 1D Wigner crystal remains in each DW but inter-DW coherence vanishes, similar to the transition from 2D crystalline state to 2D smectic state seen in liquid crystals. A smectic liquid crystal-like phase is confirmed by the 2D FFT plots of Fig. 4m–p that exhibit trivial peaks because of the periodic DW line array (marked with red circles) as well as a nontrivial feature (marked by blue ovals) that arise because of the interior 1D Wigner crystal periodicity. Intensity within each blue oval reflects a constant wavevector along the DW direction (corresponding to the 1D Wigner crystal periodicity), but the diffuseness of the feature reflects randomness in the direction perpendicular to the DW and thus indicates disorder between different Wigner crystal chains. These diffraction patterns are characteristic of more conventional smectic liquid crystal phases[10,41,42] (further data can be seen in Supplementary Information section 8).

This 2D crystalline-to-smectic transition originates from the interplay between intra- and inter-DW interactions, as well as defect-induced intra-DW potential fluctuations. At low electron densities,

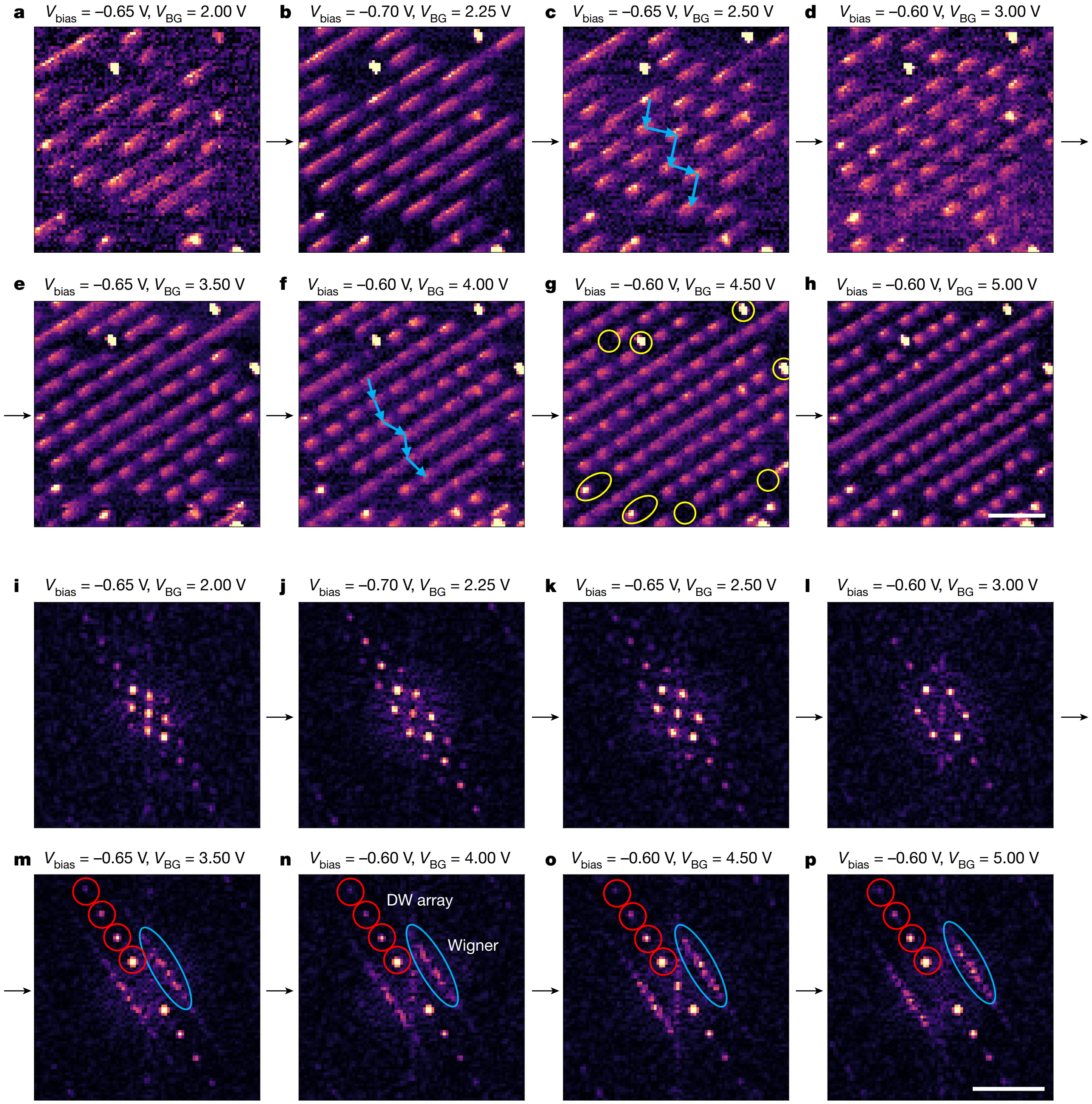

Fig. 4 | Electron crystalline-to-smectic transition in 1D DW array. a–h, CBE tunnel current maps for a periodic array of 1D DWs as V_{BG} is increased from 2.0 V to 5.0 V. Defects are marked with yellow circles in **g**. At low electron density (**a**–**d**), an array of 1D Wigner crystals is seen, which exhibits a staggered structure, forming a new 2D crystalline phase. At high electron density (**e**–**h**), the staggered order is lost and spatial coherence between nearby 1D Wigner crystals disappears, forming a new electronic smectic phase. Blue arrows label the positions of electrons in nearest-neighbour DWs. **i**–**p**, 2D FFT plots of the images shown in **a**–**h**. Hamming windows are used for the 2D FFT. At low density (**i**–**l**), the staggered Wigner crystal array yields well-defined peaks in the FFTs because of the presence of 2D crystalline structure. At high density (**m**–**p**), two features dominate the 2D FFT plots: (1) peaks reflecting the periodic spacing of DW lines (labelled with red circles); and (2) diffuse lines (labelled with blue ovals) that reflect 1D Wigner crystal periodicity but lack inter-DW spatial coherence (that is, the smectic liquid crystal state). Scale bars, 20 nm (**a**–**h**); 2 nm^{-1} (**i**–**p**).

we expect the inter-DW interaction (E_{inter}) and intra-DW interaction (E_{intra}) to both be higher than the defect-induced fluctuation potential (E_{D}). Together they stabilize the anisotropic 2D electron lattice composed of phase-locked 1D Wigner crystals that exhibit a staggered electron configuration with weak distortions to accommodate disorder. For increased electron density, however, the inter-DW interaction is expected to rapidly decrease as $E_{\mathrm{inter}} \propto e^{-\sqrt{2}\pi n l}$, where $n = N/L$ is the 1D chain electron density and l is the distance between adjacent DWs (see Supplementary Information section 9 for details). Here a new energy hierarchy emerges in which $E_{\mathrm{intra}} > E_{\mathrm{D}} > E_{\mathrm{inter}}$, causing the Wigner crystal within each chain to remain stabilized while inter-chain coherence is destroyed by disorder.

Conclusions

In conclusion, we show that layer-stacking DWs arising from differential uniaxial strain in van der Waals heterostructures offer tremendous opportunities to explore Luttinger liquid physics. Although we used the simple 2D semiconductor WS_2 as a model system here, similar isolated DWs and periodic DW arrays can be realized in any 2D bilayers with uniaxial heterostrain. A wide variety of exotic Luttinger liquid phenomena could emerge from DWs in new van der Waals heterostructures, such as 2D charge density wave materials, 2D magnets and 2D superconductors.

Online content

Any methods, additional references, Nature Portfolio reporting summaries, source data, extended data, supplementary information, acknowledgements, peer review information; details of author contributions and competing interests; and statements of data and code availability are available at https://doi.org/10.1038/s41586-024-07596-6.

1. Imambekov, A., Schmidt, T. L. & Glazman, L. I. One-dimensional quantum liquids: beyond the Luttinger liquid paradigm. *Rev. Mod. Phys.* **84**, 1253–1306 (2012).
2. Haldane, F. D. M. Effective harmonic-fluid approach to low-energy properties of one-dimensional quantum fluids. *Phys. Rev. Lett.* **47**, 1840–1843 (1981).
3. Haldane, F. D. M. 'Luttinger liquid theory' of one-dimensional quantum fluids. I. Properties of the Luttinger model and their extension to the general 1D interacting spinless Fermi gas. *J. Phys. C Solid State Phys.* **14**, 2585–2610 (1981).
4. Voit, J. One-dimensional Fermi liquids. *Rep. Prog. Phys.* **58**, 977–1116 (1995).
5. Baym, G. & Pethick, C. *Landau Fermi-Liquid Theory: Concepts and Applications* (Wiley, 2008).
6. Nozieres, P. *Theory of Interacting Fermi Systems* (CRC Press, 2018).
7. Fiete, G. A., Le Hur, K. & Balents, L. Coulomb drag between two spin-incoherent Luttinger liquids. *Phys. Rev. B* **73**, 165104 (2006).
8. Fiete, G. A. *Colloquium*: the spin-incoherent Luttinger liquid. *Rev. Mod. Phys.* **79**, 801–820 (2007).
9. Moskovtsev, K. & Dykman, M. Mobility of a spatially modulated electron liquid on the helium surface. *Phys. Rev. B* **101**, 245435 (2020).
10. Reichhardt, C. & Reichhardt, C. J. O. Collective dynamics and defect generation for Wigner crystal ratchets. *Phys. Rev. B* **108**, 155131 (2023)
11. Teo, J. C. Y. & Kane, C. L. From Luttinger liquid to non-Abelian quantum Hall states. *Phys. Rev. B* **89**, 085101 (2014).
12. Mukhopadhyay, R., Kane, C. L. & Lubensky, T. C. Sliding Luttinger liquid phases. *Phys. Rev. B* **64**, 045120 (2001).
13. Ohtsubo, Y. et al. Surface Tomonaga-Luttinger-liquid state on Bi/InSb(001). *Phys. Rev. Lett.* **115**, 256404 (2015).
14. Jompol, Y. et al. Probing spin-charge separation in a Tomonaga-Luttinger liquid. *Science* **325**, 597–601 (2009).
15. Shapir, I. et al. Imaging the electronic Wigner crystal in one dimension. *Science* **364**, 870–875 (2019).
16. Bockrath, M. et al. Luttinger-liquid behaviour in carbon nanotubes. *Nature* **397**, 598–601 (1999).
17. Ishii, H. et al. Direct observation of Tomonaga–Luttinger-liquid state in carbon nanotubes at low temperatures. *Nature* **426**, 540–544 (2003).
18. Lee, J. et al. Real space imaging of one-dimensional standing waves: direct evidence for a Luttinger liquid. *Phys. Rev. Lett.* **93**, 166403 (2004).
19. Chang, A. Chiral Luttinger liquids at the fractional quantum Hall edge. *Rev. Mod. Phys.* **75**, 1449–1505 (2003).
20. Wen, X.-G. Chiral Luttinger liquid and the edge excitations in the fractional quantum Hall states. *Phys. Rev. B* **41**, 12838–12844 (1990).
21. Stühler, R. et al. Tomonaga–Luttinger liquid in the edge channels of a quantum spin Hall insulator. *Nat. Phys.* **16**, 47–51 (2020).
22. Li, T. et al. Observation of a helical Luttinger liquid in InAs/GaSb quantum spin Hall edges. *Phys. Rev. Lett.* **115**, 136804 (2015).
23. Zhu, T. et al. Imaging gate-tunable Tomonaga–Luttinger liquids in 1H-MoSe2 mirror twin boundaries. *Nat. Mater.* **21**, 748–753 (2022).
24. Jolie, W. et al. Tomonaga-Luttinger liquid in a box: electrons confined within MoS_2 mirror-twin boundaries. *Phys. Rev. X* **9**, 011055 (2019).
25. Deshpande, V. V. & Bockrath, M. The one-dimensional Wigner crystal in carbon nanotubes. *Nat. Phys.* **4**, 314–318 (2008).
26. Emery, V. J., Kivelson, S. A. & Zachar, O. Spin-gap proximity effect mechanism of high-temperature superconductivity. *Phys. Rev. B* **56**, 6120–6147 (1997).
27. Wang, P. et al. One-dimensional Luttinger liquids in a two-dimensional moiré lattice. *Nature* **605**, 57–62 (2022).
28. Li, H. et al. Imaging moiré flat bands in three-dimensional reconstructed WSe_2/WS_2 superlattices. *Nat. Mater.* **20**, 945–950 (2021).
29. Schweizer, P., Dolle, C. & Spiecker, E. In situ manipulation and switching of dislocations in bilayer graphene. *Sci. Adv.* **4**, eaat4712 (2018).
30. Alden, J. S. et al. Strain solitons and topological defects in bilayer graphene. *Proc. Natl Acad. Sci. USA* **110**, 11256–11260 (2013).
31. Rupp, A. et al. Imaging lattice reconstruction in homobilayers and heterobilayers of transition metal dichalcogenides. *2D Mater.* **10**, 045028 (2023).
32. Kim, J. H. et al. Interface-driven partial dislocation formation in 2D heterostructures. *Adv. Mater.* **31**, 1807486 (2019).
33. Shabani, S. et al. Deep moiré potentials in twisted transition metal dichalcogenide bilayers. *Nat. Phys.* **17**, 720–725 (2021).
34. Edelberg, D., Kumar, H., Shenoy, V., Ochoa, H. & Pasupathy, A. N. Tunable strain soliton networks confine electrons in van der Waals materials. *Nat. Phys.* **16**, 1097–1102 (2020).
35. Weston, A. et al. Atomic reconstruction in twisted bilayers of transition metal dichalcogenides. *Nat. Nanotechnol.* **15**, 592–597 (2020).
36. Li, H. et al. Wigner molecular crystals from multi-electron moiré artificial atoms. Preprint at arxiv.org/abs/2312.07607 (2023).
37. Vu, D. & Sarma, S. D. One-dimensional few-electron effective Wigner crystal in quantum and classical regimes. *Phys. Rev. B* **101**, 125113 (2020).
38. Drummond, N. & Needs, R. Phase diagram of the low-density two-dimensional homogeneous electron gas. *Phys. Rev. Lett.* **102**, 126402 (2009).
39. Ceperley, D. Ground state of the fermion one-component plasma: a Monte Carlo study in two and three dimensions. *Phys. Rev. B* **18**, 3126–3138 (1978).
40. Tanatar, B. & Ceperley, D. M. Ground state of the two-dimensional electron gas. *Phys. Rev. B* **39**, 5005–5016 (1989).
41. Piro, O. E., Echeverría, G. A. & Cukiernik, F. D. Crystallography and the liquid crystal phase: a new approach to structural studies on a thermo-tropic smectic Schiff base. *Crystallogr. Rev.* **24**, 3–21 (2018).
42. de Vries, A. A structural classification of smectic liquid crystals. *Mol. Cryst. Liq. Cryst.* **63**, 215–229 (1981).

Methods

Sample fabrication

The bilayer WS_2 device was fabricated using a micromechanical stacking technique[43]. A poly(propylene) carbonate (PPC) film stamp was used to pick up all exfoliated 2D material flakes. The 2D material layers in the main heterostructure region were picked up in the following order: substrate hBN, graphite, bottom hBN, monolayer WS_2, second monolayer WS_2 (with 60° twist) and graphene nanoribbon array. The graphene nanoribbon array serves as a contact electrode for the twisted WS_2. The PPC film and stacked sample were peeled together, flipped over and transferred onto an Si/SiO_2 substrate (SiO_2 thickness 285 nm). The PPC layer was subsequently removed using ultrahigh vacuum annealing at 330 °C, resulting in an atomically clean heterostructure suitable for STM measurements. Metal layers (50 nm Au and 5 nm Cr) were evaporated through a shadow mask to form electrical contacts with graphene layers. Some residues on the shadow mask are occasionally transferred to the sample surfaces during the evaporation. These residues are later cleaned by the STM tip scratching. The STM tip is further cleaned on the GNR surface through field emission and/or tip bias pulse.

STM measurement

Tunnel current and dI/dV spectrum measurements were performed under open-loop conditions with the tip height first stabilized at tip bias V_{bias} and setpoint current I_{sp} with closed feedback and then lowered by turning off the feedback and reducing the tip height by a distance of h_{tip}. A bias modulation with 25 mV amplitude and 500–900 Hz frequency was applied to obtain the dI/dV signal. All STM measurements were performed at $T = 5.4$ K.

DW atomic structure

The DW atomic structure depends on the angle θ between the DW direction and the Burgers vector. Two extreme configurations are for shear ($\theta = 0$) and tensile ($\theta = \pi/2$) DWs (refs. 29,30). The shear DW atomic structure is shown in Extended Data Fig. 1 and shows a DW separating two AB stacking regions. Here a guide to the eye shows the W atoms in the bottom layer (orange dots) and the S atoms in the top layer (blue dots) across the DW to help visualize the interlayer dislocation. Although the S and W atoms are on top of one another to the left of the DW, they are separated by a unit cell to the right of the DW. Most DWs observed in this work have a Burgers vector angle θ between 0 and π/2, as identified through surface topography and atomically resolved STM images (for example, see Supplementary Fig. 1).

CBE tunnel current measurement

In this work, we probe the DW-correlated electrons using the CBE tunnel current instead of the conventional scanning tunnelling spectroscopy (STS).

Conventionally, the STS measures the sample density of states at the energy of the tip bias (with respect to the sample Fermi level). To measure the electronic states around the Fermi level (in which most of the interesting correlated states live), dI/dV spectra around zero tip bias need to be measured that reflect the density of states at the Fermi level. However, a known difficulty hindering the conventional STS study of correlated states in TMD semiconductors is the difference in the large tip and sample work function. At zero bias, the work function difference induces charge accumulation at the tip apex that generates a strong local electric field and hence a local band bending effect in the probed TMD layer (analogous to the origin of the Schottky barrier in the metal–semiconductor interface). This local band bending can destroy the fragile correlated states locally and prohibit the measurement of their intrinsic properties.

To overcome the above issue, we discard the conventional STS measurement scheme and instead choose to measure the CBE tunnel current that can minimize the tip perturbation, as described below.

Here we apply a proper sample-tip bias (Extended Data Fig. 2a) to satisfy two requirements simultaneously:

1. Alignment of the tip chemical potential μ_{tip} within the WS_2 bandgap. As the chemical potential of electron-doped WS_2 (μ_{tip}) lies above the CBE, when the tip chemical potential is lowered into the WS_2 band gap, the tunnel current (denoted CBE tunnel current) comes only from the doped WS_2 CBE electrons.
2. Alignment of the tip and WS_2 vacuum energy levels. This is to compensate for the work function difference between the tip and WS_2 and ensure minimal tip perturbation to interacting electrons in the DW. Experimentally, we achieve this by finding V_{bias} that yields the best imaging quality (indicating alignment of the sample and tip vacuum levels and minimized tip perturbation) (see Supplementary Information section 5 for details). We note that the previously carefully prepared STM tip was used to probe partially filled Landau levels with minimum perturbation close to zero tip bias[44]. Here the large-tip-WS_2 work function difference requires a nonzero tip bias to minimize the tip perturbation.

The CBE tunnel current map directly reflects the spatial distribution of doped electrons as demonstrated previously in CBE current measurements on Wigner molecular crystals in moire artificial atoms[36]. Extended Data Fig. 2b shows the tunnel current I–V characteristic on a log scale as a function of V_{BG} measured at the centre of a DW with a large tip and sample separation (determined by the setpoint condition of $V_{\mathrm{bias}} = -3.30$ V, $I_{\mathrm{sp}} = 20$ pA and $\mathrm{h}_{\mathrm{tip}} = -50$ pm; see Methods on STM measurement). Negligible tunnel current occurs for $-1.8\ \mathrm{V} < V_{\mathrm{bias}} < 0$, which corresponds to the WS_2 semiconducting band gap (the valence band edge (VBE) and CBE are marked with white dashed lines). The CBE tunnel current is lower than the measurement noise floor in the bandgap region because of the large tip and sample separation. When the tip height is slightly lowered (setpoint condition: $V_{\mathrm{bias}} = -2.70$ V, $I_{\mathrm{sp}} = 20$ pA and $h_{\mathrm{tip}} = -100$ pm), the CBE tunnel current starts showing up in the gap region, as seen in Extended Data Fig. 2c. Ideally, the tunnel current is expected to be constant (zero dI/dV) within the band gap while experimentally a bias-dependent current variation (nonzero dI/dV) is still observed because of the presence of tip perturbation at non-ideal tip bias. Here dispersing features appear in the range $3\ \mathrm{V} < V_{\mathrm{BG}} < 8$ V that correspond to quantized electron number changes in a finite-length 1D Wigner crystal (see additional details in Supplementary Information section 10).

Thermal excitation and spin-incoherent Luttinger liquid

We can gain insight into how thermal excitation affects the spin degree of freedom by considering the energetics of a 1D chain of electrons compared with the thermal background. At lower densities, the electrons are far apart with reduced wavefunction overlap and so the spin exchange energy is strongly suppressed. This is reflected in the DMRG-calculated spin excitation energy E_J (that is, the energy to flip a single spin in an 80-nm long electron chain; see Supplementary Information section 7 for details), which is plotted in Extended Data Fig. 3a and shows exponential reduction with separation for $n < 0.30\ \mathrm{nm}^{-1}$. This is much smaller than the charge excitation energy $\hbar\omega_0$ (that is, the zero-momentum longitudinal optical phonon energy of a 1D Wigner crystal; see Supplementary Information section 7 for details). For $n < 0.30\ \mathrm{nm}^{-1}$, the thermal energy k_BT at $T = 5.4$ K dominates over the spin energy, thus precluding any possible spin coherence.

Wigner crystal dimerization and magneto-elastic coupling

The Wigner crystal dimerization occurs when the spin exchange energy E_J exceeds the thermal energy k_BT, thus making the spin behaviour important in the Wigner crystal. In this regime, the electrons are antiferromagnetically coupled and the exchange energy E_J strongly depends on the electron separation d (Extended Data Fig. 3b). This causes magneto-elastic coupling between the spin and charge of the Wigner crystal, as described by the expression[7]

$$H_{s-c} = J_1 \sum_l (u_{l+1} - u_l) \boldsymbol{S}_{l+1} \cdot \boldsymbol{S}_l.$$

Here $J_1 = \partial J/\partial d$, where J is the spin exchange interaction (which is related to E_J, see Supplementary Information section 7), and u_l and $\mathbf{S}_l$ are the spatial coordinates and spin of the lth electron. This spin–lattice interaction term is similar to what is seen in spin-Peierls systems[45,46], except that the phonon originates from an electron lattice rather than an atomic lattice. Magneto-elastic coupling lowers the overall energy of the 1D system by dimerizing the lattice to gain magnetic energy (Extended Data Fig. 3b), thus enhancing the $2k_F$ density oscillation as J_1 increases at higher electron density. This order is expected to decay algebraically from the defects pinning the crystal. However, a quantitative analysis of the algebraic decay is challenging in the experiment because of the limited signal-to-noise ratio.

Evidence for the magnetic origin of the dimerization phenomenon can be further seen by calculating the entanglement entropy S_{EE} of the 1D electron chain. S_{EE} reflects the degree of entanglement for adjacent electrons and so provides a measure of spin-singlet formation. Extended Data Fig. 3c shows the DMRG calculation of entanglement entropy S_{EE} across each site of the electron chain at $n = 0.3\ \text{nm}^{-1}$ (see Supplementary Information section 6 for details). A clear oscillation in the entanglement entropy is observed, suggesting a high degree of entanglement between each dimerized electron pair and thus a tendency towards spin-singlet formation. The combination of spin–lattice coupling and alternating valence bond order in the dimerized 1D Wigner crystal is analogous to the physics of 1D polyacetylene as described by the Su–Schrieffer–Heeger model[47].

Data availability

The data supporting the findings of this study can be found at GitHub (https://github.com/HongyuanLiCMP/Imaging-Tunable-Luttinger-Liquid-Systems-in-van-der-Waals-Heterostructures) and are also available from the corresponding authors upon reasonable request.

43. Wang, L. et al. One-dimensional electrical contact to a two-dimensional material. *Science* **342**, 614–617 (2013).
44. Farahi, G. et al. Broken symmetries and excitation spectra of interacting electrons in partially filled Landau levels. *Nat. Phys.* **19**, 1482–1488 (2023).
45. Bray, J. W. et al. Observation of a spin-Peierls transition in a Heisenberg antiferromagnetic linear-chain system. *Phys. Rev. Lett.* **35**, 744–747 (1975).
46. Cross, M. C. & Fisher, D. S. A new theory of the spin-Peierls transition with special relevance to the experiments on TTFCuBDT. *Phys. Rev. B* **19**, 402–419 (1979).
47. Su, W. P., Schrieffer, J. R. & Heeger, A. J. Solitons in polyacetylene. *Phys. Rev. Lett.* **42**, 1698–1701 (1979).

Acknowledgements This work was primarily funded by the US Department of Energy, Office of Science, Basic Energy Sciences, Materials Sciences and Engineering Division under contract no. DE-AC02-05-CH11231 within the van der Waals heterostructure programme KCFW16 (device fabrication, STM spectroscopy, theoretical analyses and computations). Support was also provided by the National Science Foundation Award DMR-2221750 (surface preparation). This research used the Lawrencium computational cluster provided by the Lawrence Berkeley National Laboratory (supported by the US Department of Energy, Office of Basic Energy Sciences, under contract no. DE-AC02-05-CH11231). S.T. acknowledges primary support from the US Department of Energy SC0020653 (materials synthesis), NSF CMMI1825594 (NMR and TEM studies on crystals), NSF DMR-1955889 (magnetic measurements on crystals), NSF ECCS2052527 (bulk electrical tests), DMR 2111812 and CMMI 2129412 (optical tests on bulk crystals). K.W. and T.T. acknowledge support from the JSPS KAKENHI (grant nos. 21H05233 and 23H02052) and the World Premier International Research Center Initiative (WPI), MEXT, Japan. H.L. acknowledges support from Kavli Energy Nano Sciences Institute graduate student fellowship. We acknowledge the Texas Advanced Computing Center (TACC) at the University of Texas at Austin for providing high-performance computing resources. This research also used resources of the National Energy Research Scientific Computing Center (NERSC), a US Department of Energy, Office of Science User Facility, located at Lawrence Berkeley National Laboratory, operated under contract no. DE-AC02-05CH11231.

Author contributions H.L., M.P.Z., M.F.C. and F.W. conceived the project. H.L., Z.X., J.N. and S.L. fabricated the WS_2 heterostructure device. H.L. and Z.X. performed the STM/STS measurement of the WS_2 device. T.W. and M.P.Z. performed the DMRG calculations of the 1D interacting electrons. M.H.N., W.K. and S.G.L. performed the ab initio calculations of the DW structures. Z.G. and Z.H. performed the measurement of the QPI in bilayer $MoSe_2$. H.L., Z.X., A.Z., M.F.C. and F.W. discussed the experimental design and analysed the experimental data. Y.O., R.B. and S.T. grew the WS_2 crystals. K.W. and T.T. grew the hBN single crystal. All authors discussed the results and wrote the paper.

Competing interests The authors declare no competing interests.

Additional information

Supplementary information The online version contains supplementary material available at https://doi.org/10.1038/s41586-024-07596-6.

Correspondence and requests for materials should be addressed to Hongyuan Li, Steven G. Louie, Michael P. Zaletel, Michael F. Crommie or Feng Wang.

Peer review information *Nature* thanks Wouter Jolie and the other, anonymous, reviewer(s) for their contribution to the peer review of this work.

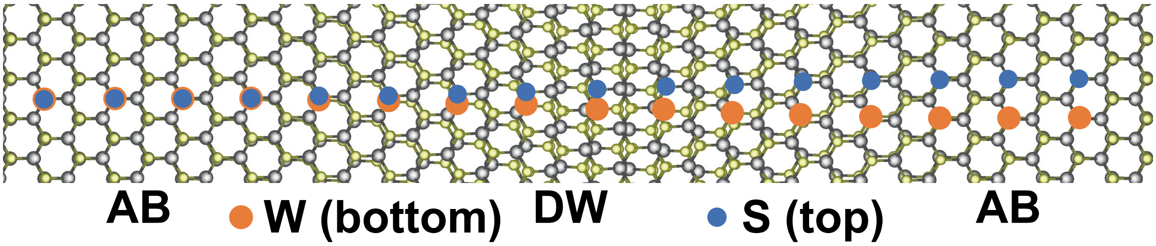

Extended Data Fig. 1 | Sketch of the atomic structure for a shear-type stacking DW. The left and right regions are AB stacked while the center shows a vertically aligned DW. The positions of W atoms in the bottom layer (orange dots) and S atoms in the top layer (blue dots) are highlighted along a linecut across the DW. For shear-type DWs, the two AB stacking regions have an interlayer unit-vector shift parallel to the DW.

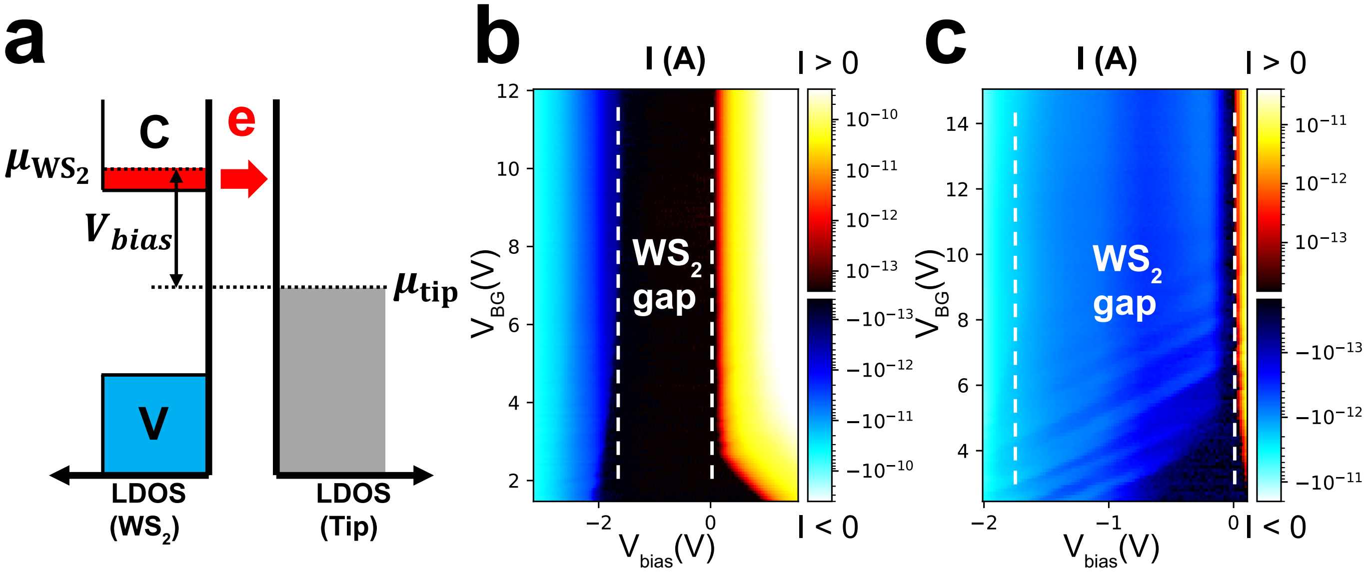

Extended Data Fig. 2 | Conduction band edge tunnel current measurement. **a**. Schematic energy diagram for the conduction band edge (CBE) tunnel current measurement of electron-doped WS$_2$. The WS$_2$ chemical potential μ_{WS_2} lies above the CBE. When the tip chemical potential μ_{tip} (controlled by V_{bias}) is the aligned within the band gap of the WS$_2$, the tunnel current arises from the doped electrons at the conduction band edge. **b,c**. Tunnel current I-V characteristics as a function of V_{BG} measured at the DW center for electron-doped WS$_2$ with (**b**) a large ($V_{bias} = -3.30$ V, $I_{sp} = 20$ pA, $h_{tip} = -50$ pm) and (**c**) small ($V_{bias} = -2.70$ V, $I_{sp} = 20$ pA, $h_{tip} = -100$ pm) tip-sample separation. The current is plotted on a log scale with the positive and negative branches using different colormaps. The CBE and valence band edge (VBE) are marked with white dashed lines. For small tip-sample separation a negative CBE tunnel current can be seen in the WS$_2$ gap.

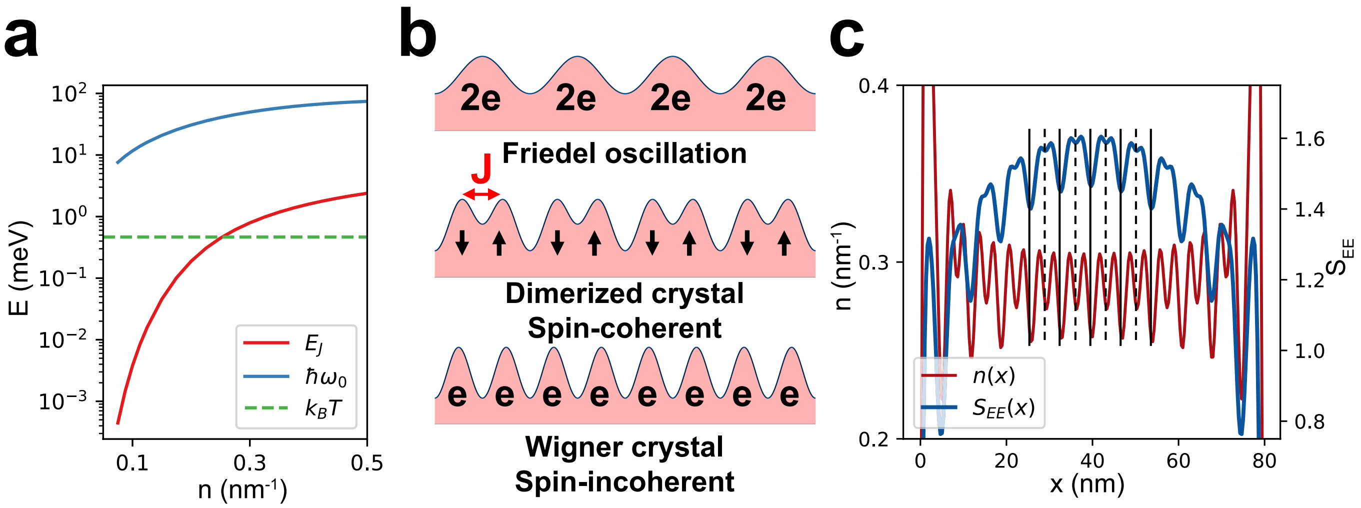

Extended Data Fig. 3 | Analysis of the Wigner-Friedel crossover. a. Calculated charge phonon energy $\hbar\omega_0$ and exchange interaction energy E_J as a function of 1D chain electron density. The experimental temperature energy scale is labeled with a green dashed line. **b**. Schematic illustration of 1D electron chain with decreasing interaction strength (from bottom to top) shows three regimes: Wigner crystal, dimerized crystal, and Friedel oscillation. **c**. DMRG calculation of the charge density $n(x)$ and entanglement entropy S_{EE} across each site of 1D electron chain for n = 0.3 nm^{-1} (see SI section 6 for details). S_{EE} reflects the degree of entanglement (and therefore singlet formation) between neighboring electrons in a dimerized Wigner crystal. Vertical lines label the boundary (solid) and center (dashed) of singlet pairs.